Journal of Computational Physics 318 (2016) 373–390

Contents lists available at ScienceDirect

Journal of Computational Physics

www.elsevier.com/locate/jcp

A NURBS-based generalized finite element scheme for 3D simulation of heterogeneous materials

Masoud Safdari [a], Ahmad R. Najafi [b], Nancy R. Sottos [c], Philippe H. Geubelle [a,*]

[a] Department of Aerospace Engineering, University of Illinois, Urbana, IL 61801, USA
[b] Department of Mechanical Science and Engineering, University of Illinois, Urbana, IL 61801, USA
[c] Department of Materials Science and Engineering, University of Illinois, Urbana, IL 61801, USA

ARTICLE INFO

Article history:
Received 23 June 2015
Received in revised form 21 April 2016
Accepted 2 May 2016
Available online 6 May 2016

Keywords:
NURBS
G/XFEM
Material interfaces

ABSTRACT

A 3D NURBS-based interface-enriched generalized finite element method (NIGFEM) is introduced to solve problems with complex discontinuous gradient fields observed in the analysis of heterogeneous materials. The method utilizes simple structured meshes of hexahedral elements that do not necessarily conform to the material interfaces in heterogeneous materials. By avoiding the creation of conforming meshes used in conventional FEM, the NIGFEM leads to significant simplification of the mesh generation process. To achieve an accurate solution in elements that are crossed by material interfaces, the NIGFEM utilizes Non-Uniform Rational B-Splines (NURBS) to enrich the solution field locally. The accuracy and convergence of the NIGFEM are tested by solving a benchmark problem. We observe that the NIGFEM preserves an optimal rate of convergence, and provides additional advantages including the accurate capture of the solution fields in the vicinity of material interfaces and the built-in capability for hierarchical mesh refinement. Finally, the use of the NIGFEM in the computational analysis of heterogeneous materials is discussed.

1. Introduction

The performance of materials is often linked to their microstructure, and the predictive modeling of the structure/property relationship for the complex materials has long been a topic of interest in the computational mechanics community. One of the key challenges in this line of work is associated with complexity of the microstructure. While the finite element method has emerged as the method of choice due primarily to its flexibility, the accurate capture of complex microstructure using meshes that conform to the material interfaces constitutes a challenging and time-consuming task, often representing over 80% of the total analysis time [1]. This is especially true when a large number of virtual models have to be created to capture the statistical nature of the microstructure geometry.

Of particular interest in the current work is the direct conversion of actual microstructural information to FE models. Substantial progress has been achieved over the past two decades in the development of robust and efficient algorithms that allow converting the voxel arrays associated with images to structured and unstructured FE models. Some of these approaches rely on the direct voxel-to-element translation to create a structured grid of hexahedral elements [2–4]. While this approach is particularly attractive due to its simplicity and robustness, it tends to create staircase representations of

* Corresponding author. Tel./fax: +1 217 244 7648.
E-mail address: geubelle@illinois.edu (P.H. Geubelle).

http://dx.doi.org/10.1016/j.jcp.2016.05.004
0021-9991/

material interfaces [5], which might affect the solution unless an extremely refined (and computationally expensive) finite element model is adopted [4]. Another approach, based on discrete representation of the material interfaces combined with the generation of unstructured finite element meshes that conform to these interfaces [6,5,7], has shown to represent more accurately the geometrical details of the interface. However, the generation of conformal meshes is tedious and far from robust especially for a 3D domain with complex material interfaces [8], and it often requires sophisticated tools [9]. These methods usually regularize material interfaces, limit the discretization to tetrahedral elements, and require user intervention. Further, they lead to meshes containing degenerate [6,5] and poorly shaped elements with high aspect ratios [10]. Many research activities have focused on enhancing the robustness and accuracy of these methods [11–13,8]. However, although they tend to improve the resulting mesh quality, these techniques also tend to lead to very large finite element discretizations.

To address these issues and move some of the complexity from computational geometry to the finite element formulation, generalized (extended) finite element methods (G/XFEM) [14–21], unfitted FEM [22], and CutFEM [23] have been suggested that avoid the need for conforming mesh generation. Among these techniques, we highlight a recently developed generalized finite element method, referred to as Interface-enriched Generalized Finite Element Method or IGFEM [24,25], which allows for the capture of material interfaces using meshes that do not conform to the materials microstructure. In this method, the additional degrees of freedom (dofs) are introduced along the intersections of the material interfaces with the edges of the non-conforming mesh and linear Lagrangian basis is used as enrichment. This method has recently been extended to NURBS-based Interface-enriched Generalized Finite Method (NIGFEM) [26,27], which incorporates directly into the finite element formulation the NURBS representation of the surfaces defining the material interfaces. Non-Uniform Rational B-Splines (NURBS) [28,29] are used widely in CAD to represent complex geometries. By incorporating directly the NURBS representation into the finite element formulation of the non-conforming elements intersected by the material interfaces, the NIGFEM greatly simplifies the mesh generation process while providing the same accuracy and convergence properties as those of conventional FEM based on conforming meshes. Similar ideas were presented in the context of regular FEM [30] and G/XFEM [31,32].

In addition to easing the mesh generation for complex geometries, NIGFEM, like its G/XFEM counterparts, can simplify the meshing step for problems involving moving boundaries and continuous geometrical and topological changes [33,34], thereby avoiding complex and costly adaptive remeshing. The use of hexahedral elements, which are usually preferred to tetrahedral elements in structural problems [35], is another advantage of the proposed method for investigating 3D problems with complex geometries.

In this study, we extend the NIGFEM to 3D modeling of heterogeneous materials and investigate its properties. In Section 2, we discuss the formulation of NIGFEM for structural problems. This section starts with a brief introduction to NURBS and its key properties. We then discuss the construction of NURBS-based enrichment functions utilized by NIGFEM and associated finite element formulation. In Section 3, we present a detailed convergence study of NIGFEM. In the last section, we provide two application problems to illustrate the efficiency and accuracy of the method.

2. Formulation and implementation

2.1. Brief introduction to NURBS

NURBS are one of the most common and powerful methods adopted by the computer-aided design (CAD) community to represent complex curves, surfaces and volumes. For completeness, we provide hereafter a brief review of NURBS formulation based on [29,28]. A univariate NURBS curve is defined by

$$\boldsymbol{C}(\xi) = \frac{\sum_{i=1}^{n} N_{i,p}(\xi) w_i \boldsymbol{P}_i}{\sum_{i=1}^{n} N_{i,p}(\xi) w_i}, \tag{1}$$

where $\boldsymbol{P}_i$ are the *control points*, w_i are the *weights* ($w_i > 0$), and $N_{i,p}$ are the B-spline basis functions, where p is the polynomial degree and n is the number of basis functions (and also number of control points). The polygon formed by $\boldsymbol{P}_i$ is called *control polygon* (see Fig. 1-a). The basis functions are evaluated at ξ which takes values in the interval of a knot vector Ξ. A knot-vector is a set of $n + p + 1$ non-decreasing real numbers representing coordinates in a parametric space. The interval of knot vector is arbitrary, but it is commonly normalized to $[0, 1]$. A knot vector is said to be *open* if its first and last knot values are repeated $p + 1$ times as

$$\Xi = \{\underbrace{0, \ldots, 0}_{\text{p+1}}, \xi_{p+2}, \ldots, \xi_n, \underbrace{1, \ldots, 1}_{\text{p+1}}\}. \tag{2}$$

Open knot vectors are often adopted by CAD systems. The interval $[\xi_i, \xi_{i+1})$ is called a *knot span*. B-spline basis functions are defined recursively as

$$N_{i,0}(\xi) = \begin{cases} 1 & \xi_i \le \xi < \xi_{i+1} \\ 0 & \text{otherwise} \end{cases}, \tag{3}$$

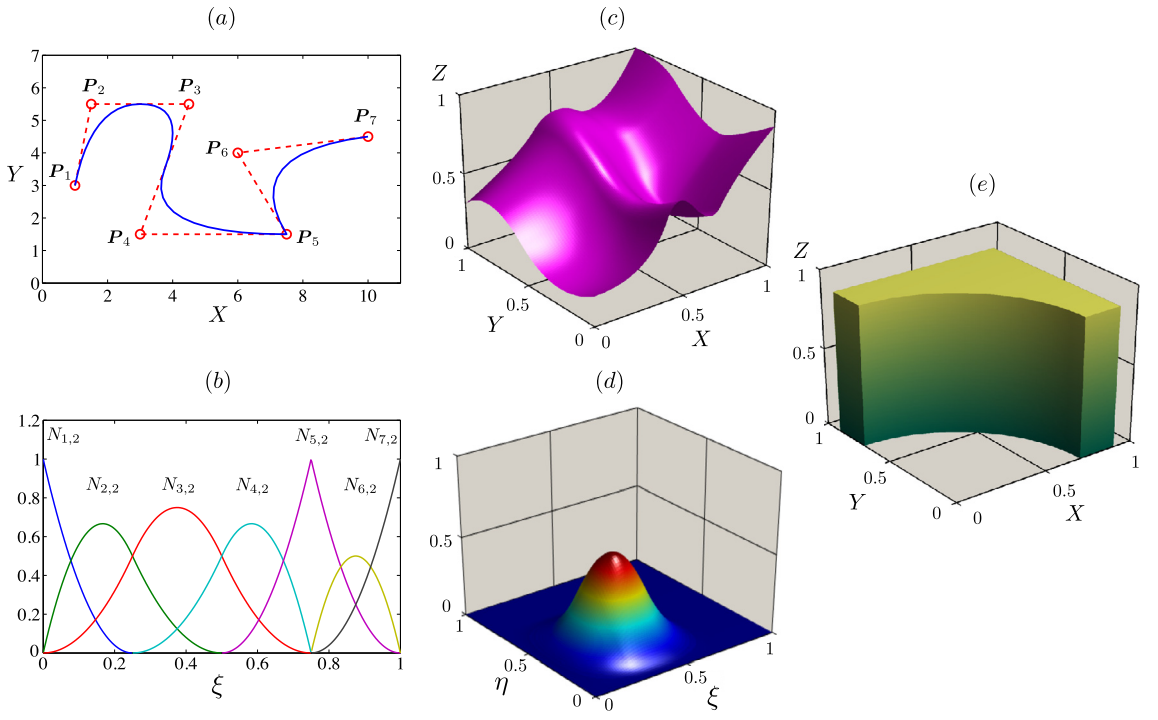

Fig. 1. (a–b) A quadratic ($p = 2$) NURBS curve constructed by seven control points $\boldsymbol{P}_i$ (control polygon shown with dashed line), the knot vector $\Xi = \{0, 0, 0, 1/4, 1/2, 3/4, 3/4, 1, 1, 1\}$ and its B-spline basis functions $N_{i,2}(\xi)$ $(i = 1 \dots 7)$. (c–d) A bi-quadratic ($p = q = 2$) NURBS surface constructed by 6×6 control points and one of its basis functions ($N_{3,2}(\xi) \times N_{3,2}(\eta)$) corresponding to $\boldsymbol{P}_{3,3}$. (e) A bi-quadratic/linear ($p = q = 2$, $r = 1$) NURBS volume (solid) constructed by $4 \times 4 \times 2$ control points.

and

$$N_{i,p}(\xi) = \frac{\xi - \xi_i}{\xi_{i+p} - \xi_i} N_{i,p-1}(\xi) + \frac{\xi_{i+p+1} - \xi}{\xi_{i+p+1} - \xi_{i+1}} N_{i+1,p-1}(\xi), \ (p > 0). \tag{4}$$

Note that the support of $N_{i,p}$ is limited to the interval $[\xi_i, \xi_{i+p+1})$ and $N_{i,p} = 0$ outside this interval. In general, $N_{i,p}$ is C^{p-1}-continuous when there are no repeated knots in its interval of support and, if a knot has multiplicity k, the basis functions are C^{p-k}-continuous for that knot value. Other than their compact support and controllable continuity, the most notable properties of B-spline basis functions are their non-negativity ($N_{i,p}(\xi) \neq 0$), partition of unity ($\sum_{i=1}^{n} N_{i,p}(\xi) = 1$), and linear independence. NURBS curves inherit all of the continuity properties of their bases. A quadratic NURBS curve and its corresponding basis functions are depicted in Figs. 1-a and b, respectively. Note that C^0-continuity in the curve at $\boldsymbol{P}_5$ directly results from the discontinuity of its corresponding B-spline basis function $N_{5,2}$ which is dictated by the multiplicity of the underlying knot vector at $\xi_6 = \xi_7 = 3/4$. Further, this $k = 2$ $(k = p)$ multiplicity also requires the curve to interpolate the control point at $\boldsymbol{P}_5$. Similarly, a $k = 3$ $(k = p + 1)$ multiplicity at the beginning and the end of the knot vector requires the curve to (i) interpolate the initial and final control points and (ii) start and end at these points (C^{-1}-continuity). Key properties of NURBS curves include their convex hull (NURBS curve lies within the convex hull of its control points), affine covariance (the transform of a NURBS curve only needs to be applied to its control points), and variation diminishing (a NURBS curve can not cross a line more times than its control polygon).

Higher-order NURBS geometries also inherit most of the properties of the NURBS curves. A NURBS surface is defined by taking two knot vectors and a bidirectional $(n \times m)$ control net $\boldsymbol{P}_{i,j}$ through

$$\boldsymbol{S}(\xi, \eta) = \sum_{i=1}^{n} \sum_{j=1}^{m} R_{i,j}^{(p,q)}(\xi, \eta) \boldsymbol{P}_{i,j}, \tag{5}$$

where $R_{i,j}^{(p,q)}$ basis is a tensor product between two sets of pth and qth-order piecewise B-spline basis functions

$$R_{i,j}^{(p,q)}(\xi, \eta) = \frac{N_{i,p}(\xi) N_{j,q}(\eta) w_{i,j}}{\sum_{i_1=1}^{n} \sum_{j_1=1}^{m} N_{i_1,p}(\xi) N_{j_1,q}(\eta) w_{i_1,j_1}}. \tag{6}$$

Some of the properties of $R_{i,j}^{(p,q)}$ are their local support $[\xi_i, \xi_{i+p+1}) \times [\eta_j, \eta_{j+q+1})$, non-negativity and the partition of unity $\sum_{i=1}^{n}\sum_{j=1}^{m} R_{i,j}^{p,q}(\xi,\eta) = 1$ for all $(\xi,\eta) \in [0,1] \times [0,1]$. A sample bi-quadratic NURBS surface and one of its basis functions are shown in Figs. 1-c and d, respectively. A NURBS volume (or solid) is a subset of $\mathbb{R}^3$ which includes surfaces and internal points of an object. A NURBS volume is a trivariate parametric representation constructed from a tridirectional mesh ($n \times m \times l$) of control points $\boldsymbol{P}_{i,j,k}$ and three knot vectors by

$$\boldsymbol{V}(\xi,\eta,\zeta) = \sum_{i=1}^{n}\sum_{j=1}^{m}\sum_{k=1}^{l} R_{i,j,k}^{(p,q,r)}(\xi,\eta,\zeta)\boldsymbol{P}_{i,j,k}, \tag{7}$$

where the $R_{i,j,k}^{(p,q,r)}$ basis function is again defined by taking the tensor product between three sets of pth, qth and rth-order piecewise B-spline basis functions defined by

$$R_{i,j,k}^{(p,q,r)}(\xi,\eta,\zeta) = \frac{N_{i,p}(\xi)N_{j,q}(\eta)N_{k,r}(\zeta)w_{i,j,k}}{\sum_{i_1=1}^{n}\sum_{j_1=1}^{m}\sum_{k_1=1}^{l} N_{i_1,p}(\xi)N_{j_1,q}(\eta)N_{k_1,r}(\zeta)w_{i_1,j_1,k_1}}. \tag{8}$$

Again, $R_{i,j,k}^{(p,q,r)}$ preserves all of the properties of univariate and bivariate B-spline basis functions as well as compact support $[\xi_i, \xi_{i+p+1}) \times [\eta_j, \eta_{j+q+1}) \times [\zeta_k, \zeta_{k+r+1})$, non-negativity, and partition of unity. In the interior of the cuboid $[\xi_i, \xi_{i+1}) \times [\eta_j, \eta_{j+1}) \times [\zeta_k, \zeta_{k+1})$ for a knot value (ξ_0, η_0, ζ_0) with multiplicity k_1, k_2, and k_3, respectively, all partial derivatives of $R_{i,j,k}^{(p,q,r)}$ exist up to order $(p-k_1, q-k_2, r-k_3)$. A sample bi-quadratic/linear ($p = q = 2$, $r = 1$) NURBS volume is shown in Fig. 1-e. One of the properties of NURBS is their flexibility to represent singular features of a geometry. For instance, geometric singularities like sharp corners can be easily represented by NURBS. For example, the sharp corner in the geometry shown in Fig. 1-e is created by superposing a number of control points. These properties of NURBS are very useful in representing complex geometric features. In the current work, NURBS surfaces are used to represent material interfaces and NURBS volumes are used to describe subspaces of an element traversed by material interfaces.

2.2. NIGFEM formulation and enrichment functions

To present the NIGFEM formulation, we consider its application to linear elastostatics problems. Let us consider a 3D structural problem with domain $\Omega = \bigcup_{i=1}^{N_\Omega} \Omega_i \subset \mathbb{R}^3$, $\bigcap_{i=1}^{N_\Omega} \Omega_i = \emptyset$ with closure $\bar{\Omega}$ is bounded by $\partial\Omega = \bar{\Omega} - \Omega$ with outward normal vector $\mathbf{n}$, where N_Ω is the number of subdomains Ω_i, $i = 1, 2, \ldots, N_\Omega$. The boundary $\partial\Omega$ is composed of two complementary subsets Γ^t and Γ^u, i.e., $\partial\Omega = \Gamma^u \cup \Gamma^t$ and $\Gamma^u \cap \Gamma^t = \emptyset$, over which traction $\bar{\mathbf{t}}$ and displacement $\bar{\mathbf{u}}$ are prescribed. We assume that the material interfaces are smooth and are defined by $\mathbf{S} = \bigcup_{i=1}^{N_S} \mathbf{S}_i \subset \mathbb{R}^2$ and satisfy $\bigcap_{i=1}^{N_S} \mathbf{S}_i = \emptyset$, where N_S is the number of interfaces. The normal vector on each material interface $\mathbf{S}_i$ is denoted by $\mathbf{n}_i$.

The strong formulation of a elastostatics field can be expressed as

$$\nabla \cdot \boldsymbol{\sigma} + \mathbf{b} = \mathbf{0} \text{ in } \Omega, \tag{9}$$

$$\boldsymbol{\sigma} = \mathbf{C} : \boldsymbol{\varepsilon}, \tag{10}$$

$$\boldsymbol{\varepsilon} = \nabla_s \mathbf{u}, \tag{11}$$

where $\mathbf{u}$ is displacement, $\boldsymbol{\sigma}$ and $\boldsymbol{\varepsilon}$ respectively denote the stress and strain tensors, $\mathbf{C}$ is the elasticity tensor, $\mathbf{b}$ is the body force vector, and ∇_s is the symmetric gradient operator. The essential and natural boundary conditions can be formulated as

$$\mathbf{u} = \bar{\mathbf{u}} \text{ on } \Gamma^u, \tag{12}$$

$$\boldsymbol{\sigma} \cdot \mathbf{n} = \bar{\mathbf{t}} \text{ on } \Gamma^t, \tag{13}$$

where $\bar{\mathbf{u}}$ and $\bar{\mathbf{t}}$ are prescribed displacements and tractions, respectively. Interface conditions take the form:

$$[\![\boldsymbol{\sigma} \cdot \mathbf{n}_i]\!] = 0 \text{ on } \mathbf{S}_i \quad (i = 1,\ 2,\ ,\ \ldots,\ N_S), \tag{14}$$

with $[\![.]\!]$ denoting the jump symbol that indicates discontinuity of a physical quantity.

To express the weak form of the governing equation, let $\mathcal{S} = H^1(\Omega)$ be the standard Sobolev space and $\mathcal{V} = H_0^1(\Omega)$ be the standard Sobolev space of functions that vanish on Γ^u. The weak form statement is then written as

Find $\mathbf{u} \in \mathcal{S}$ such that

$$\int_\Omega \nabla\mathbf{w} : \boldsymbol{\sigma}(\mathbf{u}) d\Omega = \int_\Omega \mathbf{w} \cdot \boldsymbol{b} d\Omega + \int_{\Gamma^t} \mathbf{w} \cdot \bar{\mathbf{t}} d\Gamma, \quad \forall \mathbf{w} \in \mathcal{V}. \tag{15}$$

Now for a discrete system, let $\mathcal{S}^h \subset \mathcal{S}$ and $\mathcal{V}^h \subset \mathcal{V}$ be considered as finite dimensional subspaces, which are used as the approximation trial and test spaces. The weak form of this discrete problem can be written as

Find $\mathbf{u}^h \in \mathcal{S}^h$ such that

$$\int_{\Omega^h} \nabla \mathbf{w}^h : \boldsymbol{\sigma}(\mathbf{u}^h) d\Omega = \int_{\Omega^h} \mathbf{w}^h \cdot \boldsymbol{b} d\Omega + \int_{\Gamma^{t^h}} \mathbf{w}^h \cdot \bar{\mathbf{t}} d\Gamma, \quad \forall \mathbf{w}^h \in \mathcal{V}^h. \tag{16}$$

The finite element solution to this weak statement is obtained by discretizing the domain into N_e finite elements ($\Omega \cong \Omega^h = \bigcup_{i=1}^{N_e} \Omega_e^i$) and approximate the unknown displacement field in each element as

$$\mathbf{u}^{\mathbf{h}}(\mathbf{x}) = \sum_{i=1}^{n_e} N_i(\mathbf{x}) \mathbf{u}_i, \tag{17}$$

where $N_i(\mathbf{x})$ are the basis functions, n_e is the number of nodes in each element and $\mathbf{u_i}$ denote the vector of nodal values. The NIGFEM utilizes a non-conforming mesh for which some of the elements are traversed by material interfaces. For elements not traversed by material interfaces, the NIGFEM approximation is given by (17). However, to capture the weak discontinuity (C^0) of the solution along material interfaces, the solution field in each element intersected by an interface is locally augmented by a series of extra degrees of freedom $\boldsymbol{\alpha}_{jk}$ and enrichment functions $\psi_{jk}(\mathbf{x})$ as

$$\mathbf{u}^{\mathbf{h}}(\mathbf{x}) = \sum_{i=1}^{n_e} N_i(\mathbf{x}) \mathbf{u}_i + \sum_{j=1}^{n_{\psi_j}} \sum_{k=1}^{n_{\psi_k}} \psi_{jk}(\mathbf{x}) \boldsymbol{\alpha}_{jk}, \tag{18}$$

in which n_{ψ_j} and n_{ψ_k} are the number of enrichment functions along two parametric directions specifying a NURBS surface that represent the material interface. In the NIGFEM, Lagrangian shape functions $N_i(\mathbf{x})$ are used for the standard finite element approximation to the solution field, and NURBS are used to construct the enrichment functions $\psi_{jk}(\mathbf{x})$. While the enrichment degrees of freedom $\boldsymbol{\alpha}_{jk}$ are added to the nodes of the non-conforming mesh in conventional G/XFEM, the $\boldsymbol{\alpha}_{jk}$ are introduced along the material interface in the NIGFEM. Using NURBS as a basis for enrichment allows the NIGFEM to capture highly complex material interfaces, with the number of enrichment functions ($n_\psi = n_{\psi_j} \times n_{\psi_k}$) dictated by the level of complexity of the material interfaces.

Let us represent a material interface by a quadratic NURBS surface $\boldsymbol{S}(\xi, \eta)$. To construct the enrichment functions, we first interact $\boldsymbol{S}(\xi, \eta)$ with the domain $\boldsymbol{\Omega}^h$ (shown in Fig. 2-a), which is discretized by a structured mesh composed of tri-linear hexahedral (brick) elements $\boldsymbol{\Omega}_i^h$, $i = 1 \ldots m$. Without loss of generality, let us assume that the material interface is a straight cylinder that is normal to the plane of the non-conforming mesh, and let us consider more complex configurations later. Fig. 2-b shows possible cases in which the material interface splits an intersecting element under the mentioned assumptions. Let us represent by $\boldsymbol{S}_e$ a portion of material interface residing inside an element. The portion of a NURBS surface residing in the element ($\boldsymbol{S}_e$) is in general not a NURBS surface itself. Therefore, we must first find a NURBS approximation to $\boldsymbol{S}_e$, which we denote $\boldsymbol{S}_e^h$. There are different approaches to obtain $\boldsymbol{S}_e^h$, including global and local fitting approaches and boundary-based approaches [28]. Bilinearly blended Coons surface is one of the boundary-based techniques to construct the surface $\boldsymbol{S}_e^h$ requiring only information about the boundaries of $\boldsymbol{S}_e$ [28]. To construct a Coons surface, we label boundaries of $\boldsymbol{S}_e$ with curves $\boldsymbol{C}_i^e$ ($i = 1 \ldots 4$ in the current configuration), as shown in Fig. 2-c. Each $\boldsymbol{C}_i^e$ is created by intersecting $\boldsymbol{S}$ with the faces of the element. Since $\boldsymbol{S}$ is a bi-quadratic surface, $\boldsymbol{C}_i^e$ are generally at least quadratic. We find these quadratic NURBS curves using a global interpolation technique described in [28]. With the aid of the NURBS curves $\boldsymbol{C}_i^e$, we now construct a Coons surface $\boldsymbol{S}_e^h$ in each intersected element (as an approximation to $\boldsymbol{S}_e$) such that $\boldsymbol{S} \cong \boldsymbol{S}^h = \bigcup_{i=1}^{m_i} \boldsymbol{S}_i^h$ and m_i is the number of elements traversed by the material interface(s). $\boldsymbol{S}_e^h$ is referred to hereafter as *sub-interface*. It should be noted that the order of the Coons surface is dictated by the order of its boundary curves. We use quadratic boundary curves, so the obtained Coons surface is bi-quadratic. In the next step, we use control points and knot vectors of these sub-interfaces and some of the topological information of $\boldsymbol{\Omega}^e$ including its nodal coordinates to define the NURBS representation of the volumes $\boldsymbol{\Omega}_i^e$ (Fig. 2-d) by

$$\boldsymbol{\Omega}_i^e(\xi, \eta, \zeta) = \sum_{j=1}^{n} \sum_{k=1}^{m} \sum_{l=1}^{2} R_{j,k,l}^{(p,q,r)}(\xi, \eta, \zeta) \mathbf{P}^{\boldsymbol{i}}_{j,k,l}, \quad i = 1, 2\,. \tag{19}$$

Let us refer to $\boldsymbol{\Omega}_i^e$ as *sub-domain* in the sequel. We take n and m control points in the parametric ξ- and η-directions of the sub-domain, which are selected parallel to the sub-interface parametric directions. In the normal direction (ζ-direction), we take only two control points, the minimum number needed for a linear interpolation in this direction. Similarly, we choose in this work the order of $\boldsymbol{\Omega}_i^e$ to be $p = q = 2$ in the ξ- and η-direction and $r = 1$ in the ζ-direction. It should be noted that the order of the approximation for the basis functions is arbitrary in the NIGFEM, and, for a highly curvilinear interface, a higher-order basis may enhance the precision of the approximation. Similarly, the number of control points n ($\geq p + 1$) and m ($\geq q + 1$) can vary depending on the level of complexity of $\boldsymbol{S}_e$. To reproduce the sharp edges of $\boldsymbol{\Omega}_i^e$,

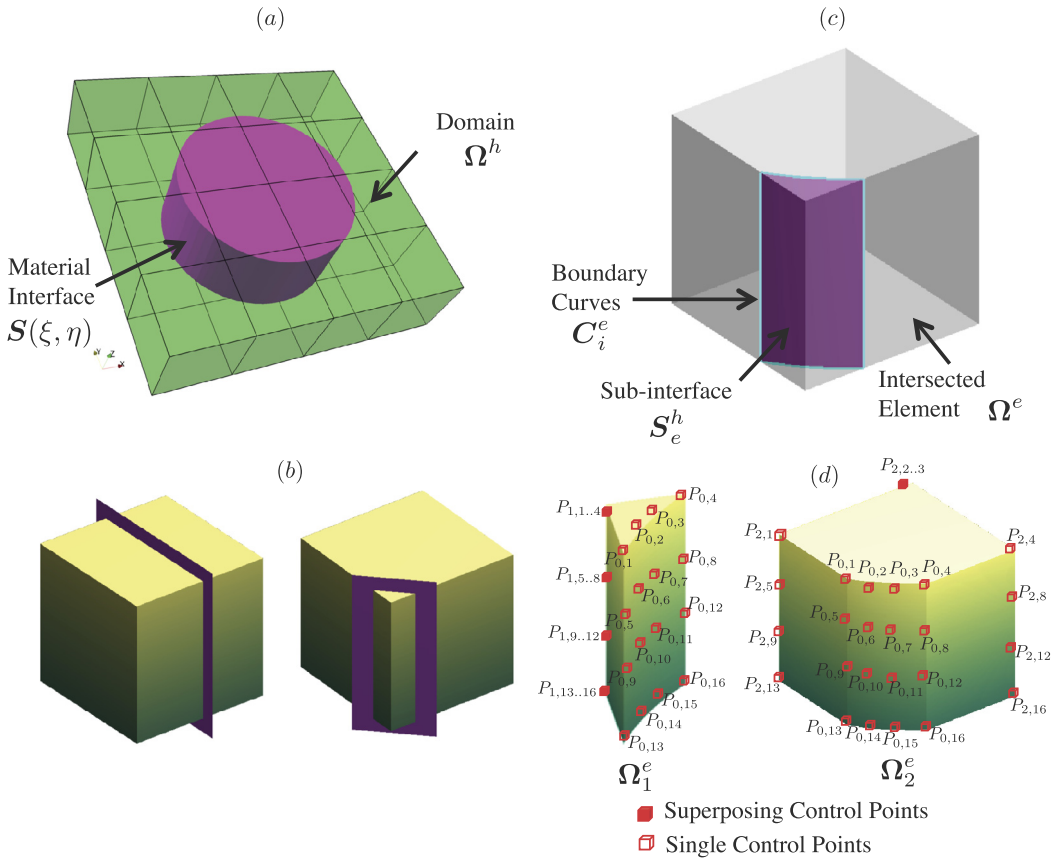

Fig. 2. (a) NIGFEM domain with a cylindrical interface $\boldsymbol{S}(\xi,\eta)$ discretized by a structured mesh of trilinear hexahedral elements; (b) two possible geometric configurations for elements traversed by the material interface; (c–d) Reconstruction of NURBS surface $\boldsymbol{S}_e^h$ from the computed boundary curves C_i^e and NURBS volume $\boldsymbol{\Omega}_i^e$, $i=1,2$ corresponding to the intersected element.

we can change the multiplicity of knot values in knot-vectors of $\boldsymbol{\Omega}_i^e$. Another approach is to adopt a normal knot vector without multiplicities and use superposing control points to create sharp corners/edges. Here, we take the latter approach to avoid changing the continuity level of the NURBS basis functions of $\boldsymbol{\Omega}_i^e$. Therefore, we choose $n=m=4$ and knot vectors $\Xi_{\xi,\eta}=\{0,0,0,0.5,1,1,1\}$ for the parametric ξ- and η-directions. Since two control points and a linear interpolation are selected for the ζ-direction, we choose $\Xi_\zeta=\{0,0,1,1\}$ as knot vector associated with this direction. Let us label the basis functions corresponding to $\boldsymbol{S}_e^h\cap\boldsymbol{\Omega}_i^e$ by $(R_{j,k,l=1})_{\boldsymbol{\Omega}_1^e}$ and $(R_{j,k,l=1})_{\boldsymbol{\Omega}_2^e}$. From the combination of these basis functions, we define

$$\psi_{jk}^e(\xi,\eta,\zeta)=\begin{cases}(R_{j,k,l=1})_{\boldsymbol{\Omega}_1^e} & (\xi,\eta,\zeta)\in\boldsymbol{\Omega}_1^e,\\ (R_{j,k,l=1})_{\boldsymbol{\Omega}_2^e} & (\xi,\eta,\zeta)\in\boldsymbol{\Omega}_2^e,\\ 0 & \text{otherwise.}\end{cases}\tag{20}$$

Note that ψ_{jk}^e $(j,k=1,2,\ldots,n_{\psi_j}=n_{\psi_k}=4)$ are non-zero only in $\boldsymbol{\Omega}^e$ and vanish everywhere else. Furthermore, these functions are C^0-continuous along material interface $\boldsymbol{S}_e^h$ because $(R_{j,k,1})_{\boldsymbol{\Omega}_1^e}=(R_{j,k,1})_{\boldsymbol{\Omega}_2^e}=1$ on $\boldsymbol{S}_e^h$. Therefore, the displacement field $\boldsymbol{u}^h$ is also C^0-continuous along these material interfaces. In the NIGFEM scheme, we take ψ_{jk}^e as enrichment to the finite element approximation space to capture gradient discontinuities existing along material interfaces. This is a natural choice because (i) these enrichment functions accurately describe the geometry of the interface, and (ii) they inherit all the needed properties for enrichment from the NURBS space including compact support, differentiability and linear independence. In the NIGFEM, we also use $\boldsymbol{\Omega}_i^e$ as the integration elements because (i) they decompose the element space into disjoint sub-domain spaces sharing the material interface and (ii) the NURBS automatically provide a map between these complex sub-domain spaces and a simple parametric space.

For more clarification, let us further explain the procedure of constructing the NURBS representation of the volume sub-domain $\boldsymbol{\Omega}_i^e$, $i=1,2$ for an intersecting element as shown in Fig. 2-d. The sixteen control points of sub-interface S_e^h, which reside in the element space, are labeled by $P_{0,j}$, $j=1,\ldots,16$. For sub-domain $\boldsymbol{\Omega}_1^e$, we also take sixteen dummy control points along the edge of $\boldsymbol{\Omega}_1^e$ parallel to the sub-interface $\boldsymbol{S}_e^h$, $P_{1,j}$, $j=1,\ldots,16$. By superposing several control

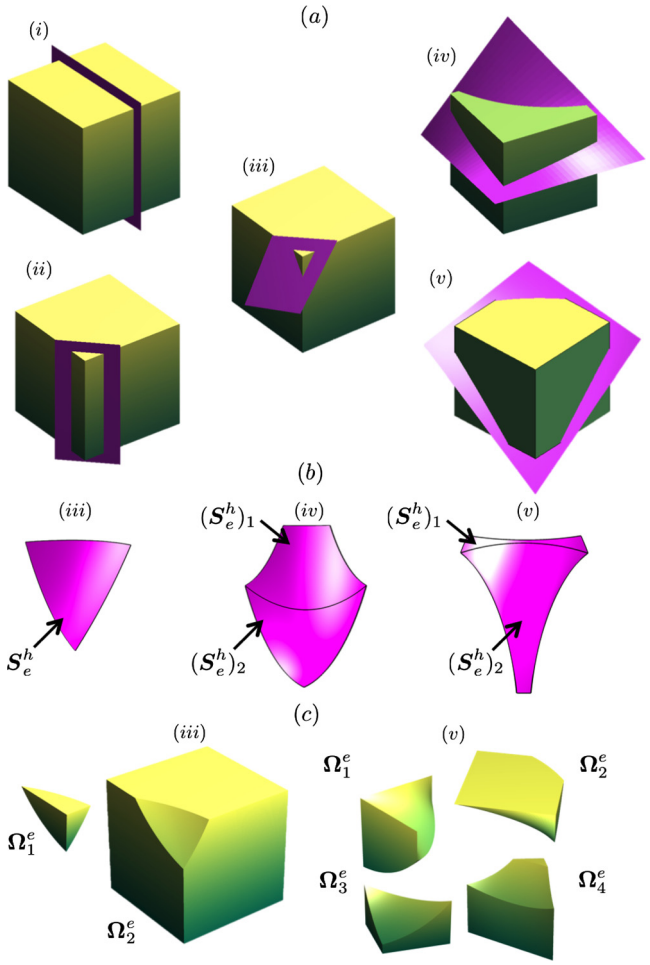

Fig. 3. (a) Five possible geometric configurations for an element traversed by a material interface. (b–c) Construction of the sub-interface $\boldsymbol{S}_e^h$ and volumetric NURBS representation of the sub-domains $\boldsymbol{\Omega}_i^e$ for geometric configurations (iii)–(v).

points, the sharp edge of the element is reproduced successfully. The superposed control points of $P_{1,1..4}$ and $P_{1,13..16}$ are coincident with the two vertices of the element $\boldsymbol{\Omega}$ and the control points in-between are selected uniformly along the edge that connects these vertices. We call these control points dummy because no dof is associated with them, and they are just used to construct NURBS volumes. With the selected control points $P_{i,j}$, $i = 0, 1$, $j = 1, \ldots, 16$ and the knot vectors $\Xi_{\xi,\eta,\zeta}$, we can create a 3D NURBS volume for $\boldsymbol{\Omega}_1^e$. We take the same approach to construct a 3D NURBS volume for $\boldsymbol{\Omega}_2^e$ using the control points $P_{i,j}$, $i = 0, 2$, $j = 1, \ldots, 16$ with the same knot vectors $\Xi_{\xi,\eta,\zeta}$.

Fig. 3-a shows more complex geometric combinations arising from interacting a material interface with a hexahedral element. In cases (i) and (ii), a four-sided $\boldsymbol{S}_e^h$ is needed, which can be readily constructed by Coons method as described earlier. For case (iii), a three-sided sub-interface needs to be constructed. In this case, we again use Coons method and, for the missing boundary curve, we define a NURBS curve that degenerates into a single point as shown in Fig. 3-b (iii). Fig. 3-c (iii) shows the associated NURBS sub-domains. The sharp corners and edges are again created by superposing several control points. Figs. 3-a (iv) and (v) show the two remaining combinations. In these cases, we create the sub-interfaces $\boldsymbol{S}_e^h$ by combining three- and four-sided Coons surfaces as respectively shown in Figs. 3-b (iv) and (v). Because of the discrete nature of $\boldsymbol{S}_e^h$ in these situations, we divide the element space into four disjoint sub-domains, as shown in Fig. 3-c (v), such that $\boldsymbol{\Omega}^e = \cup_{i=1}^4 \boldsymbol{\Omega}_i^e$.

For these complex cases, we again select $n = m = 4$ control points in the ξ and η-directions and $l = 2$ control points in ζ-direction. The order of sub-domains are also selected to be $p = q = 2$, $r = 1$. Similarly, the enrichment functions are also defined based on (20). The five geometric combinations shown in Fig. 3-a are the basic combinations accounted for in the NIGFEM. In all these cases, it is assumed that an interface cuts an element edge at most once and each element is traversed by at most one material interface. These assumptions are valid for smooth material interfaces with a reasonable level of curvature. It should be noted that, depending on the level of complexity of the material interface, other geometric combinations are possible. For instance, highly-curved material interfaces can cut an element edge more than once, or an element can be traversed by more than one material interface. In these situations, we use a local octree refinement to

resolve the situation into one the cases (i)–(v) shown in Fig. 3-a (see also the discussion on hierarchical refinement in Section 2.4).

2.3. Finite element formulation

The finite element approximation for 3D linear elastostatic problems involves solving the linear system of equations

$$\mathbb{K}\mathbb{U} = \mathbb{F}, \tag{21}$$

where $\mathbb{K}$ denotes global stiffness matrix, $\mathbb{U}$ is the vector of unknown nodal displacements, and $\mathbb{F}$ is the vector of global nodal forces. The global stiffness matrix is assembled as

$$\mathbb{K} = \mathop{\mathbb{A}}_{i=1}^{N_e} (\mathbf{K}^{\mathbf{e}})_i, \tag{22}$$

where $\mathbb{A}$ is the assembly operator, N_e is number of elements, and $(\mathbf{K}^e)_i$ is the local stiffness matrix for element i,

$$\mathbf{K}^e = \int_{\mathbf{\Omega}^e} \mathbb{B}^T(\mathbf{x})\mathbb{C}(\mathbf{x})\mathbb{B}(\mathbf{x})d\Omega, \tag{23}$$

with $\mathbb{C}(\mathbf{x})$ is the constitutive matrix at material point $\mathbf{x}$, and

$$\mathbb{B} = \begin{bmatrix} \mathbf{B}_N(\mathbf{x}) & \mathbf{B}_\psi(\mathbf{x}) \end{bmatrix}. \tag{24}$$

In (24), $\mathbf{B}_N(\mathbf{x})$ and $\mathbf{B}_\psi(\mathbf{x})$ are given by

$$\mathbf{B}_N(\mathbf{x}) = \begin{bmatrix} \frac{\partial N_1}{\partial x} & 0 & 0 & \frac{\partial N_2}{\partial x} & 0 & 0 & \dots & \frac{\partial N_{n_e}}{\partial x} & 0 & 0 \\ 0 & \frac{\partial N_1}{\partial y} & 0 & 0 & \frac{\partial N_2}{\partial y} & 0 & \dots & 0 & \frac{\partial N_{n_e}}{\partial y} & 0 \\ 0 & 0 & \frac{\partial N_1}{\partial z} & 0 & 0 & \frac{\partial N_2}{\partial z} & \dots & 0 & 0 & \frac{\partial N_{n_e}}{\partial z} \\ \frac{\partial N_1}{\partial x} & \frac{\partial N_1}{\partial y} & 0 & \frac{\partial N_2}{\partial x} & \frac{\partial N_2}{\partial y} & 0 & \dots & \frac{\partial N_{n_e}}{\partial x} & \frac{\partial N_{n_e}}{\partial y} & 0 \\ 0 & \frac{\partial N_1}{\partial y} & \frac{\partial N_1}{\partial z} & 0 & \frac{\partial N_2}{\partial y} & \frac{\partial N_2}{\partial z} & \dots & 0 & \frac{\partial N_{n_e}}{\partial y} & \frac{\partial N_{n_e}}{\partial z} \\ \frac{\partial N_1}{\partial x} & 0 & \frac{\partial N_1}{\partial z} & \frac{\partial N_2}{\partial x} & 0 & \frac{\partial N_2}{\partial z} & \dots & \frac{\partial N_{n_e}}{\partial x} & 0 & \frac{\partial N_{n_e}}{\partial z} \end{bmatrix},$$

$$\mathbf{B}_\psi(\mathbf{x}) = \begin{bmatrix} \frac{\partial \psi_{11}}{\partial x} & 0 & 0 & \frac{\partial \psi_{12}}{\partial x} & 0 & 0 & \dots & \frac{\partial \psi_{n_{\psi_j} n_{\psi_k}}}{\partial x} & 0 & 0 \\ 0 & \frac{\partial \psi_{11}}{\partial y} & 0 & 0 & \frac{\partial \psi_{12}}{\partial y} & 0 & \dots & 0 & \frac{\partial \psi_{n_{\psi_j} n_{\psi_k}}}{\partial y} & 0 \\ 0 & 0 & \frac{\partial \psi_{11}}{\partial z} & 0 & 0 & \frac{\partial \psi_{12}}{\partial z} & \dots & 0 & 0 & \frac{\partial \psi_{n_{\psi_j} n_{\psi_k}}}{\partial z} \\ \frac{\partial \psi_{11}}{\partial x} & \frac{\partial \psi_{11}}{\partial y} & 0 & \frac{\partial \psi_{12}}{\partial x} & \frac{\partial \psi_{12}}{\partial y} & 0 & \dots & \frac{\partial \psi_{n_{\psi_j} n_{\psi_k}}}{\partial x} & \frac{\partial \psi_{n_{\psi_j} n_{\psi_k}}}{\partial y} & 0 \\ 0 & \frac{\partial \psi_{11}}{\partial y} & \frac{\partial \psi_{11}}{\partial z} & 0 & \frac{\partial \psi_{12}}{\partial y} & \frac{\partial \psi_{12}}{\partial z} & \dots & 0 & \frac{\partial \psi_{n_{\psi_j} n_{\psi_k}}}{\partial y} & \frac{\partial \psi_{n_{\psi_j} n_{\psi_k}}}{\partial z} \\ \frac{\partial \psi_{11}}{\partial x} & 0 & \frac{\partial \psi_{11}}{\partial z} & \frac{\partial \psi_{12}}{\partial x} & 0 & \frac{\partial \psi_{12}}{\partial z} & \dots & \frac{\partial \psi_{n_{\psi_j} n_{\psi_k}}}{\partial x} & 0 & \frac{\partial \psi_{n_{\psi_j} n_{\psi_k}}}{\partial z} \end{bmatrix}. \tag{25}$$

By substituting (24) into (23), we obtain

$$\mathbf{K}^e = \begin{bmatrix} \mathbf{K}^e_{uu} & \mathbf{K}^e_{u\alpha} \\ \mathbf{K}^e_{\alpha u} & \mathbf{K}^e_{\alpha\alpha} \end{bmatrix}, \tag{26}$$

where

$$\mathbf{K}^e_{uu} = \sum_{i=1}^{m_s} \int_{\mathbf{\Omega}^e_i} \mathbf{B}^T_N(\mathbf{x})\mathbb{C}(\mathbf{x})\mathbf{B}_N(\mathbf{x})d\Omega,$$

$$\mathbf{K}^e_{u\alpha} = \sum_{i=1}^{m_s} \int_{\mathbf{\Omega}^e_i} \mathbf{B}^T_N(\mathbf{x})\mathbb{C}(\mathbf{x})\mathbf{B}_\psi(\mathbf{x})d\Omega,$$

$$\mathbf{K}^e_{\alpha u} = \sum_{i=1}^{m_s} \int_{\mathbf{\Omega}^e_i} \mathbf{B}^T_\psi(\mathbf{x})\mathbb{C}(\mathbf{x})\mathbf{B}_N(\mathbf{x})d\Omega,$$

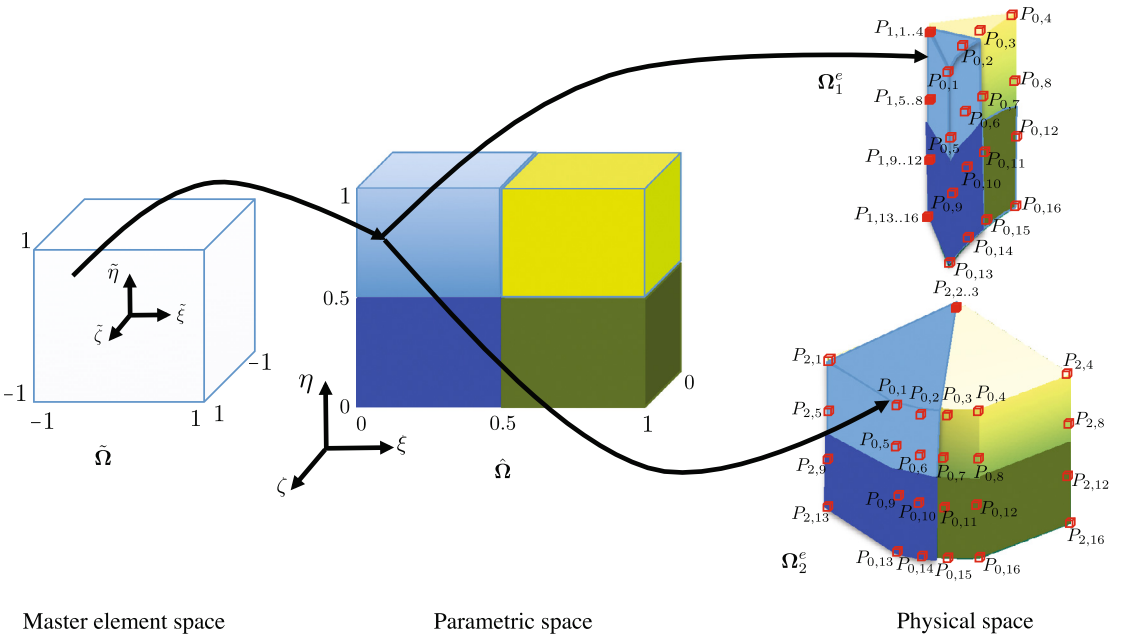

Fig. 4. Mapping used to evaluate the enriched shape function. First, the master element is mapped into a non-vanishing knot-span of the parametric space, and then is mapped into the integration element in physical domain.

$$\mathbf{K}^e_{\alpha\alpha} = \sum_{i=1}^{m_s} \int_{\mathbf{\Omega}^e_i} \mathbf{B}^T_\psi(\mathbf{x}) \mathbb{C}(\mathbf{x}) \mathbf{B}_\psi(\mathbf{x}) d\Omega, \tag{27}$$

with m_s denoting the number of subdomains in an enriched element.

These relations hold for elements that are traversed by a material interface. For all other elements, $\mathbf{B}_\psi = 0$. Similarly, we assemble the global nodal force vector from element-level contributions $\mathbf{F}^e$,

$$\mathbf{F}^e = \int_{\mathbf{\Omega}^e} \mathbb{N}^T(\mathbf{x}) \mathbf{b}(\mathbf{x}) d\Omega + \int_{\Gamma_e \cap \Gamma^t} \mathbb{N}^T(\mathbf{x}) \bar{\mathbf{t}}(\mathbf{x}) d\Gamma \tag{28}$$

where $\mathbf{b}$ and $\bar{\mathbf{t}}$ are the body force and applied traction vectors, and $\mathbb{N}$ is the shape and enrichment function vector,

$$\mathbb{N} = \begin{bmatrix} \mathbf{N}(\mathbf{x}) & \mathbf{\Psi}(\mathbf{x}) \end{bmatrix}. \tag{29}$$

Substituting (29) into (28) gives

$$\mathbf{F}^e = \begin{bmatrix} \mathbf{F}^e_u \\ \mathbf{F}^e_\alpha \end{bmatrix}, \tag{30}$$

where

$$\mathbf{F}^e_u = \sum_{i=1}^{m_s} \left[\int_{\mathbf{\Omega}^e_i} \mathbf{N}^T(\mathbf{x}) \mathbf{b}(\mathbf{x}) d\Omega + \int_{\Gamma^e_i \cap \Gamma^t} \mathbf{N}^T(\mathbf{x}) \bar{\mathbf{t}}(\mathbf{x}) d\Omega \right],$$

$$\mathbf{F}^e_\alpha = \sum_{i=1}^{m_s} \left[\int_{\mathbf{\Omega}^e_i} \mathbf{\Psi}^T(\mathbf{x}) \mathbf{b}(\mathbf{x}) d\Omega + \int_{\Gamma^e_i \cap \Gamma^t} \mathbf{\Psi}^T(\mathbf{x}) \bar{\mathbf{t}}(\mathbf{x}) d\Omega \right]. \tag{31}$$

Again, in (31), $\mathbf{F}^e_\alpha \neq 0$ only for elements traversed by material interface. For numerical integration purpose, in (27) and (31), we use the element sub-domains as integration elements. Therefore, $m = 2$ for cases (i)–(iii) and $m = 4$ for cases (iv)–(v) shown in Fig. 3-a. This way, for each $\mathbf{\Omega}^e_i$, we use the map between the NURBS parametric space and the physical space. Subsequently, we use the span-wise mapping scheme described in [26] to compute the integrals appearing in (27) and (31). In this approach, the NURBS volumes constructed in an intersected element are directly used to perform the numerical integration of the weak form. To better understand the integration process, the mapping for an enriched element of case (ii) in Fig. 3-a is illustrated in Fig. 4. As apparent there, the integrals are pulled back, first onto the parametric space $\hat{\Omega}$ and then each non-vanishing knot-span of each NURBS volume in parametric space $\hat{\Omega}$ onto a bi-unit master element $\tilde{\Omega}$. We perform these integrations by Gaussian quadrature using a classical change of variables formulation.

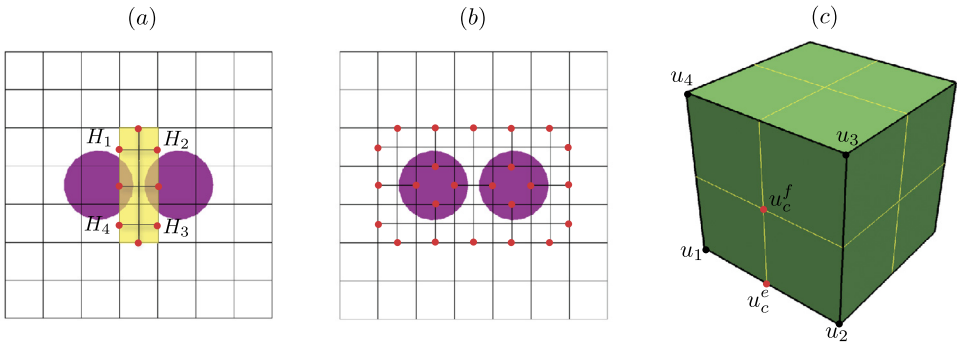

Fig. 5. (a) A 2D structured mesh highlighting elements crossed by more than one material interface. (b) A hierarchically refined mesh suggested the same problem featuring hanging nodes. (c) The octree scheme used to refine hexahedral elements used in the 3D NIGFEM to treat elements with more than one embedded material interface. (For interpretation of the references to color in this figure, the reader is referred to the web version of this article.)

2.4. Hierarchical mesh refinement

The geometric configurations illustrated in Fig. 3-a are derived based on the assumption that every enriched element is only traversed by a single material interface. Depending on the density of the structured nonconforming mesh, and the number and maximum curvature level of the material interfaces used for a NIGFEM analysis, there can be cases in which some of the elements in the mesh contain more than one material interface. For these elements, we employ a hierarchical local mesh refinement scheme, and recursively decompose some of the elements to resolve one material interface per element condition. The adopted hierarchical mesh refinement scheme leads to irregular meshes with hanging nodes. Utilization of irregular meshes with hanging nodes is also reported in other G/XFEM studies [36–38] generally to resolve steep gradients and enhance the precision of FE approximation locally.

In this section, the treatment of irregular meshes and hanging nodes used in the NIGFEM is briefly described. A more detailed discussion about different types of hanging nodes and their treatment in G/XFEM analyses can be found in [38]. In general, there are two approaches in the analysis of hanging nodes based on whether or not additional degrees of freedom are introduced to the problem. In the first approach, the shape functions of the elements containing hanging nodes are modified to provide a conforming approximation within the boundaries of elements that contain hanging nodes. The conforming shape functions can be defined readily using the approach described elsewhere [39]. A drawback for this method is the need for domain decomposition techniques during numerical integration as altered shape functions are only C^0-continuous at their support. In the second approach, often referred to as *constrained approximation*, hanging nodes are first treated as regular nodes, allowing for regular integration and assembly procedures. A set of algebraic equations is then used to constrain the DOFs associated to the hanging nodes to the regular DOFs. In the present NIGFEM study, we use the latter approach to treat hanging nodes arising from adopted hierarchical local mesh refinement scheme.

The adopted hierarchical mesh refinement scheme operates on 3D meshes. However, for illustration purpose, it is easier to show the method in a 2D setting. Fig. 5-a illustrates a 2D example in which the highlighted elements contain more than one material interface. Therefore, we need to perform a local mesh refinement to satisfy the one material interface per element assumption. Here, refinement to three highlighted elements results in introducing hanging nodes H_1 to H_4 that are shared between two enriched elements (Fig. 5-a). For these hanging nodes, proper enforcement of the constraints that ensure C^0-continuity across enriched elements is not trivial. To avoid this situation, we continue the refinement in the vicinity of these elements to make sure each hanging node is only shared between an enriched element and a standard one, as shown in Fig. 5-b, where red dots denote the hanging nodes. After the required number of refinement levels, we finally obtain a mesh for which all of the enriched elements fall within one of the cases (i)–(v) shown in Fig. 3-a. In NIGFEM, the elements that require refinement are decomposed into eight equal sized hexahedral element using an octree scheme shown in Fig. 5-c.

For an irregular mesh of this type, the irregularity index k denotes the maximum difference of refinement levels between adjacent elements in the mesh. Here, a *1-irregular* mesh ($k = 1$) is enough to satisfy the single interface per enriched element condition, but sometimes a higher level refinement ($k > 1$) is needed. A higher refinement level is also suggested for very close interfaces because steep gradients are usually expected there. As shown in Fig. 5-c, two types of hanging nodes are possible. In this example $\boldsymbol{u_c^e}$ is the edge type and $\boldsymbol{u_c^f}$ is the face type hanging nodes and u_i ($i = 1 \cdots 4$) are regular nodes used to constraint these hanging nodes. For a refined mesh with nodal set I, $I_c^e \subset I$ and $I_c^f \subset I$ are two subsets ($I_c^f \cup I_c^e = I_c \subset I$) that contain the edge and face type hanging nodes. The degrees of freedom associated to these hanging nodes are constrained to their neighboring corner nodes by

$$\boldsymbol{u_c} = \begin{cases} \frac{1}{2}\boldsymbol{u_i} + \frac{1}{2}\boldsymbol{u_j}, & i, j \in Q_c^e, c \in I_c^e \\ \frac{1}{4}\boldsymbol{u_i} + \frac{1}{4}\boldsymbol{u_j} + \frac{1}{4}\boldsymbol{u_k} + \frac{1}{4}\boldsymbol{u_l}, & i, j, k, l \in Q_c^f, c \in I_c^f \end{cases} \tag{32}$$

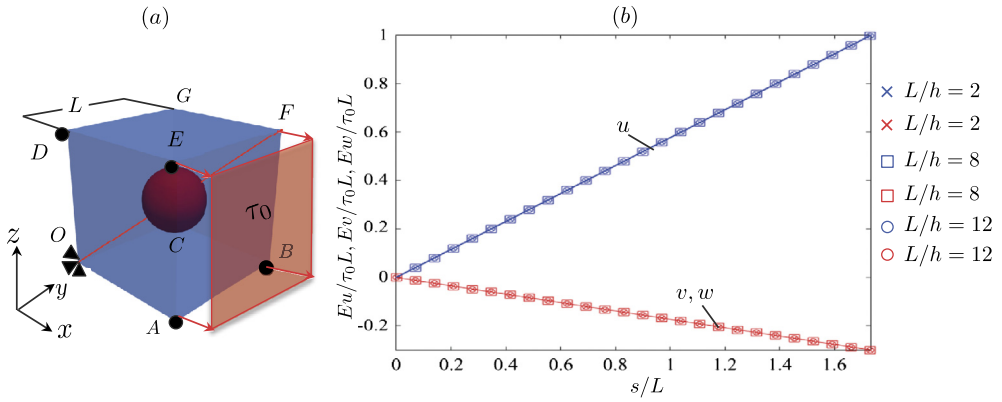

Fig. 6. (a) Domain geometry and boundary conditions used in the patch test. (b) Exact displacements along line OF captured by NIGFEM patch test.

where Q_c^e and Q_c^f are the subsets of the nodes which share the edge/face with the hanging node u_c, respectively. To enforce these algebraic constraints to the FE system of equations, we adopt the connectivity matrix method. Following [38], for each regular node a, $\boldsymbol{\pi_a}$ is a zero vector with 1 in the position a. For hanging nodes $a \in I_c$, $\boldsymbol{\pi_a}$ is defined as

$$\boldsymbol{\pi_a} = \begin{cases} [0, \ldots, \underbrace{1/2}_{i}, \ldots, \underbrace{1/2}_{j}, \ldots, 0]^T & i, j \in Q_a^e, a \in I_c^e, \\ [0, \ldots, \underbrace{1/4}_{i}, \ldots, \underbrace{1/4}_{j}, \ldots, \underbrace{1/4}_{k}, \ldots, \underbrace{1/4}_{l}, \ldots, 0]^T & i, j, k, l \in Q_a^f, a \in I_c^f. \end{cases} \tag{33}$$

We assemble $\boldsymbol{\pi_a}$ for all nodes into the square matrix

$$\boldsymbol{\pi}^* = \{\boldsymbol{\pi_1}, \ldots, \boldsymbol{\pi_n}\}, \tag{34}$$

where n is the total number of nodes including regular and hanging nodes. We then eliminate all of zero-valued rows (belonging to hanging nodes) from $\boldsymbol{\pi}^*$ to obtain the global connectivity matrix $\boldsymbol{\pi}$, thereby reducing (21) to

$$\boldsymbol{\pi} \cdot \mathbb{K} \cdot \boldsymbol{\pi}^T \cdot \mathbb{U}_r = \boldsymbol{\pi} \cdot \mathbb{F}, \tag{35}$$

where $\mathbb{U}_r$ is the displacement vector for all regular nodes. The final solution vector which contains both regular and hanging node solutions is then obtained by

$$\mathbb{U} = \boldsymbol{\pi}^T \cdot \mathbb{U}_r. \tag{36}$$

3. Convergence and accuracy

3.1. Patch test

We start this convergence study of the NIGFEM by performing a patch test. The domain and boundary conditions for this first example are presented in Fig. 6-a. The domain consists of a cubic matrix with a side length L containing a spherical inclusion with the radius a ($a/L = 0.23$). The domain is pinned at corner O and subjected to a uniform traction τ_0, normal to face $ABEF$, while symmetry boundary conditions are applied to faces $OACB$, $OCDG$ to ensure a uniaxial state of stress in the x-direction and to avoid rigid body motion. Assuming the same elastic material properties, E and ν, for the matrix and the inclusion, the exact solution is

$$(u, v, w) = \left(\frac{\tau_0}{E}x, -\frac{\nu\tau_0}{E}y, -\frac{\nu\tau_0}{E}z\right), \tag{37}$$

which, as shown in Fig. 6-b, is reproduced exactly by the NIGFEM.

3.2. Convergence

To investigate the convergence and accuracy of the NIGFEM, the displacement and stress fields around a spherical inclusion (of stiffness E_2 and Poisson's ratio ν_2) embedded in an infinite domain (with properties E_1 and ν_1) subject to a far-field uniaxial state of stress σ_0 are computed. In this problem, the NIGFEM solution is compared against standard FE solution. The errors are calculated by comparing NIGFEM and FE approximation with an analytical solution [40] using the L_2-norm of the error for the displacement and stress fields defined by

$$\|e_u\|_{L_2} = \left[\int_{\Omega} (\mathbf{u} - \mathbf{u}^h)^T (\mathbf{u} - \mathbf{u}^h) d\Omega \right]^{1/2}, \tag{38}$$

$$\|e_\sigma\|_{L_2} = \left[\int_{\Omega} (\boldsymbol{\sigma} - \boldsymbol{\sigma}^h)^T (\boldsymbol{\sigma} - \boldsymbol{\sigma}^h) d\Omega \right]^{1/2}, \tag{39}$$

where $\mathbf{u}$ and $\boldsymbol{\sigma}$ are respectively the exact displacement and stress fields and $\mathbf{u}^h$ and $\boldsymbol{\sigma}^h$ are the corresponding NIGFEM solutions. We also study the convergence of the NIGFEM in the enriched elements by computing the L_2-norm of the error for the displacement field defined over the material interface by

$$\|e_{u_S}\|_{L_2} = \left[\int_{\Omega_S} (\mathbf{u} - \mathbf{u}^h)^T (\mathbf{u} - \mathbf{u}^h) d\Omega \right]^{1/2}, \tag{40}$$

$$\|e_{\sigma_S}\|_{L_2} = \left[\int_{\Omega_{S+}} (\boldsymbol{\sigma} - \boldsymbol{\sigma}^h)^T (\boldsymbol{\sigma} - \boldsymbol{\sigma}^h) d\Omega \right]^{1/2}, \tag{41}$$

where Ω_S and Ω_{S^+} is the material interface, i.e., the surface of the spherical inclusion, and its limit approaching from the outside of the inclusion. Fig. 7-a shows the problem geometry, which consists of a cube of side length L containing a spherical inclusion with radius a ($a/L = 0.23$). The exact solution for the displacement and stress fields is obtained from the classical Goodier solution [40]. In the NIGFEM model, the spherical inclusion is represented by a second-order NURBS surface and the cubic domain is discretized into a structured mesh of hexahedral elements. The FE meshes used for the study are composed from unstructured trilinear hexahedral elements. For both NIGFEM and FE models, traction boundary conditions corresponding to the exact solution are applied to the faces of the domain to account for finite size effects. The center of the domain is pinned and the center of each face of the cube is limited to move along the normal direction using a roller support to prevent rigid-body motion.

Fig. 7-b shows rate of convergence of the L_2-norm of error for the displacements with respect to the mesh size (h) obtained by the NIGFEM and FEM. As apparent there, the NIGFEM solution preserves the optimal rate of convergence and provides a more accurate solution compared to FE. A supper-convergent patch recovery technique [41] is used to enhance the approximation quality of the gradient field for both FE and NIGFEM solutions. Fig. 7-c compares the h-dependence of the convergence rate for the L_2-norm of error for the stresses in the entire domain. It is again observed that the NIGFEM solution is more accurate for the gradient field and it preserves the optimal rate of convergence similar to standard FEM.

Figs. 7-d and e compare the quality of the NIGFEM and FEM solutions obtained along the material interface by showing the convergence of the L_2-norm of the error on the displacement and stress solutions computed along the material interface. The L_2-norm of error for the displacements along material interfaces shows that NIGFEM provides a more accurate solution along the material interface for all levels of discretization. A similar comparison of the L_2-norm of error for the stresses along the material interface, however, shows that the NIGFEM solution for stresses is only more accurate for coarse meshes. By increasing the level of refinement, the NIGFEM shows a sub-optimal rate of convergence, and for very fine meshes NIGFEM solution for stress starts to lose its accuracy. This loss in the accuracy for the finer meshes is characteristic of ill-conditioned enriched elements: as also observed in similar studies [42–45], in elements where the material interface passes very closely to one the corners of the enriched element, the condition number of the local stiffness matrix increases substantially. As the level of refinement increases, the probability of having these ill-conditioned enriched elements increases and numerical issues associated with these stiff enriched-elements hinders the rate of convergence of the gradient field approximation. Meanwhile, volumetric measures still show an optimal rate of convergence for the stress solution because the fraction of enriched elements decreases as the refinement level increase.

Figs. 8-a and b illustrate the variation of the displacement components (u^h, v^h, w^h) and stress (σ^h_{zz}, σ^h_e) along the line A–B shown in the inset for $L/h = 12$ and $E_2/E_1 = 10^{-6}$. It can be observed that, for this relatively coarse discretization, the NIGFEM solution is quite accurate. The accuracy of the NIGFEM solution for this relatively coarse non-conforming mesh is attributed to the absence of geometric errors in the model. Figs. 8-c and d show contour plots of the components of displacement w^h and stress σ^h_{zz}. As apparent in these figures, the geometry of inclusion is preserved by the non-conforming mesh. These figures also show that NURBS-based enrichment provides a higher-order approximation for the solution and its gradient in the vicinity of material interfaces.

With regards to the performance of the NIGFEM, the method involves two additional costs compared to traditional FEM: the construction of the enriched elements and the higher-order integration scheme. Based on our experience, the cost associated with constructing enriched elements is much less than the time required to make a conformal mesh, especially for complex geometries. As far as the overhead of higher-order integration scheme is concerned, we note that, since it is only associated with the enrichment elements, the higher-order integration only represents a small fraction of the total solution cost.

Compared with a regular element, an enriched element poses an extra computational cost to the analysis at the integration step. The extra computational cost associated with the numerical integration of an enriched element for elements

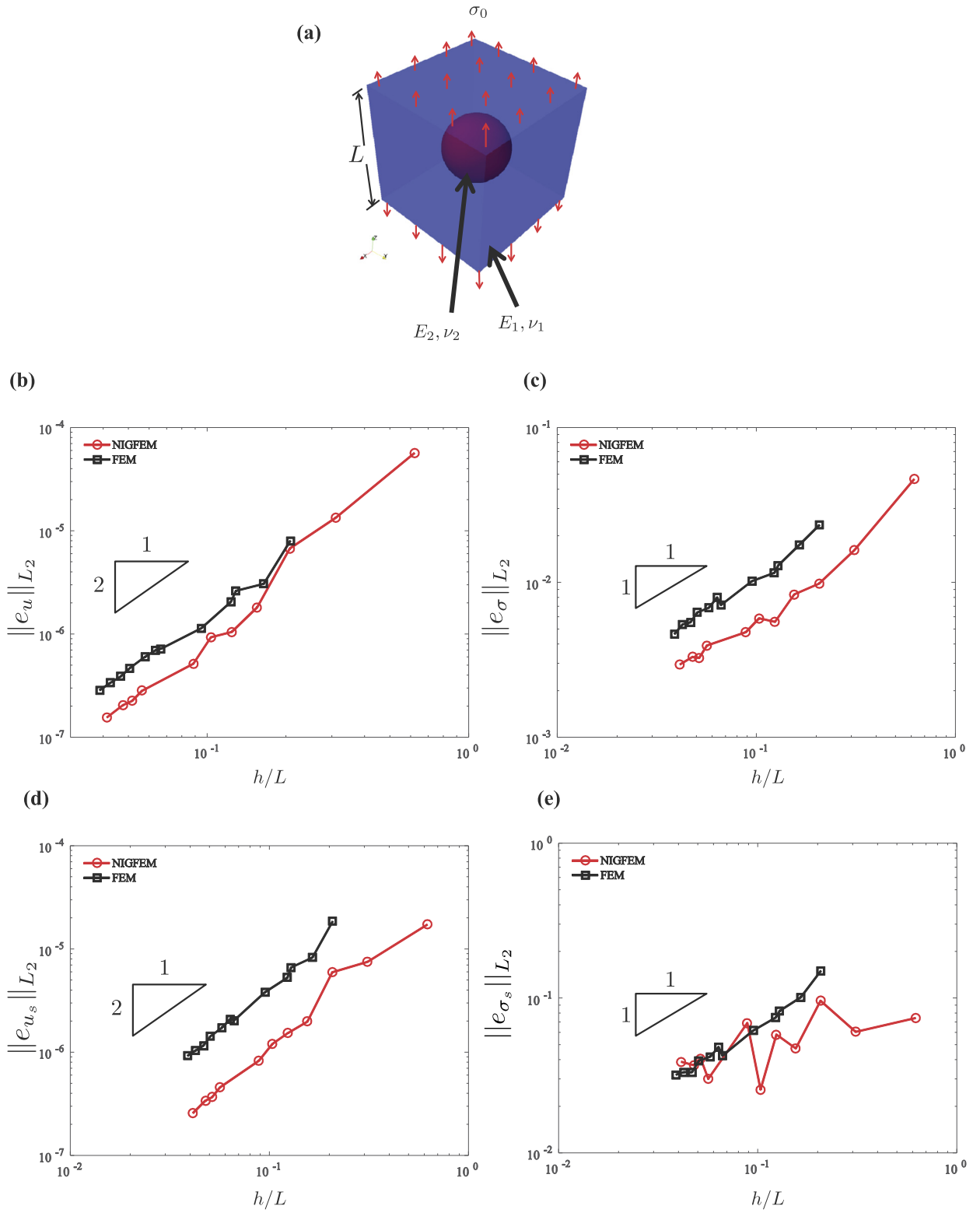

Fig. 7. (a) Domain geometry and boundary conditions used in the convergence study. Convergence rate in L_2-norm of the error for the displacement shown in (b), and stress fields shown in (c) obtained in the entire domain, and computed along the material interface shown in (d) and (e) with respect to mesh size (h) for the stiffness ratios ($E_2/E_1 = 10^{-6}$).

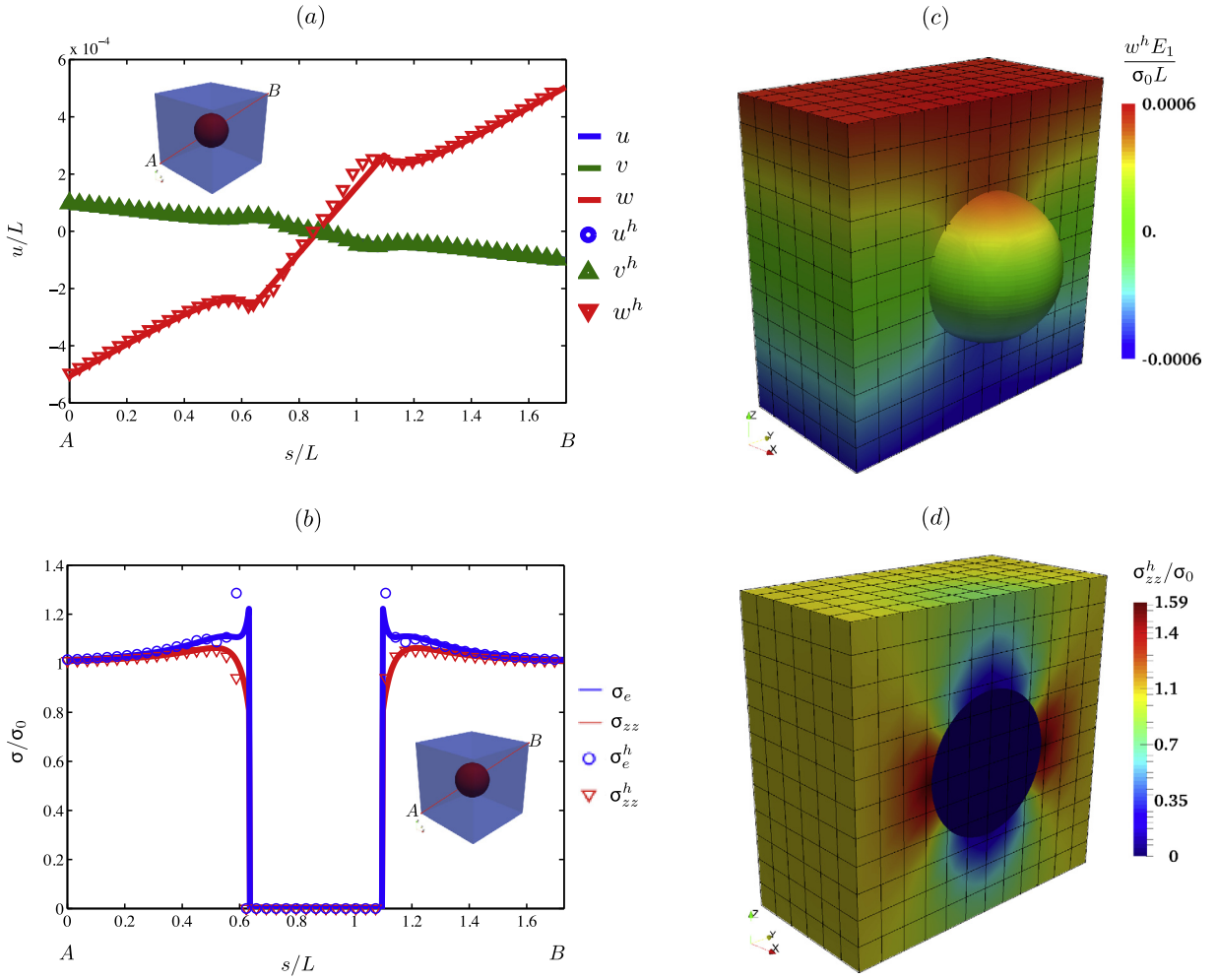

Fig. 8. Comparison between the exact (solid curve) and NIGFEM (symbols) solutions for displacements (a), stress component σ_{zz} and effective stress σ_e (b) for $E_2/E_1 = 10^{-6}$ along the line AB shown in the inset. (c–d) NIGFEM solution for displacement component w^h and stress component σ^h_{zz}.

decomposed into two sub-domains (case (i), (ii), and (iii) in Fig. 3-a) and four sub-domains (case (iv) and (v) in Fig. 3-a) with the selected knot vectors is approximately 4- and 8-times larger than that of a regular element, respectively. However, it is worth noting that usually only a small fraction of elements require enrichment, and with finer meshes this fraction tends to decrease quickly (for instance, $N_{enriched}/N_e \sim N_e^{-1/3}$ for the problem shown in Fig. 7).

4. Applications

A key application of the NIGFEM is the mesoscale analysis of materials with complex internal microstructures. In this section, the NIGFEM is used to study a series of representative structural problems involving composite media. The domain adopted in these studies involves a cube of side length L containing inclusions or cavities of various shapes. All the microstructures shown are represented with second-order NURBS surfaces.

Fig. 9 shows the domain geometry and boundary conditions for the first problem. A displacement δ is applied to the right face of the domain. Symmetry boundary conditions are used for the left, bottom and front faces and the front lower-left corner is pinned. All the other faces are traction free. Fig. 9-b illustrates the internal microstructure of the domain, which consists of a porous material composed of randomly distributed spherical cavities with varying diameter. The elastic properties are chosen as $E = 2.4$ GPa and $\nu = 0.34$. About 200 spherical cavities are randomly placed in this domain to represent the material microstructure.

Fig. 9-b also illustrates the structured, non-conforming mesh composed of 20 hexahedral elements in each direction. A one-step hierarchical refinement is introduced to resolve the condition of one material interface per element. For the selected microstructure, about 19% of the elements are refined based on the octree scheme described earlier, and the model includes 18,892 elements, 15,017 regular nodes, 11,680 hanging nodes, and 66,562 enrichment dofs after the one-step hierarchical refinement.

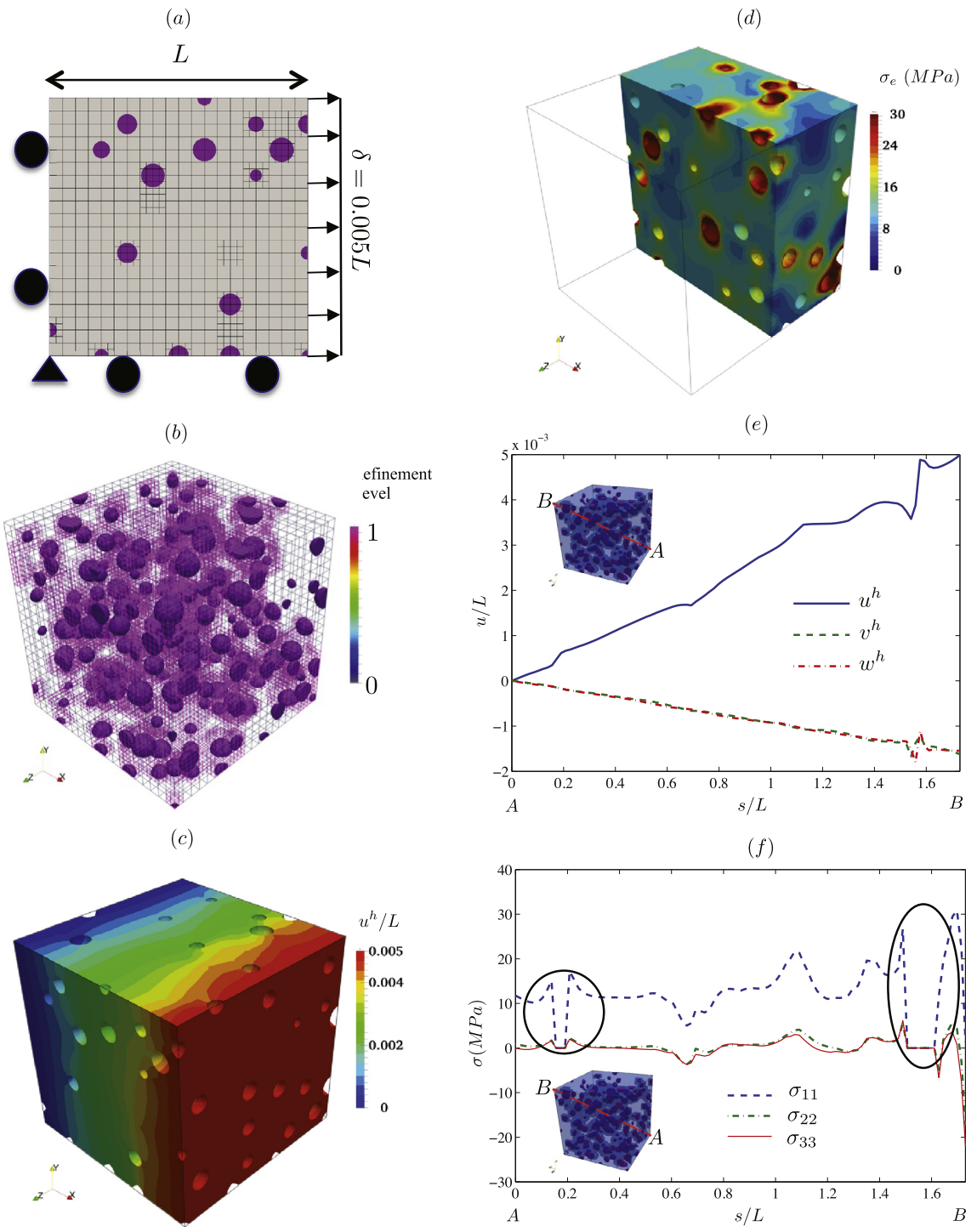

Fig. 9. (a) Domain geometry and boundary conditions for the first application problem. (b) Internal microstructure and mesh. (c–d) Contour plots for the displacement component u^h and equivalent von Mises stress σ_e obtained by NIGFEM. (e–f) NIGFEM solution for the displacements (u^h, v^h, w^h) and stress components (σ_{11}, σ_{22} and σ_{33}) along line A–B highlighted in the insets.

Figs. 9-c and d show the solution for the displacement component u^h and equivalent von Mises stress σ_e for this problem. We observe that, with a relatively coarse mesh, NIGFEM successfully preserves the material interface geometries and provides a smooth approximation to the displacement and stress fields. Figs. 9-e and f show the distribution of displacement components and stresses along a diagonal line (highlighted in the inset) which passes through some of the spherical

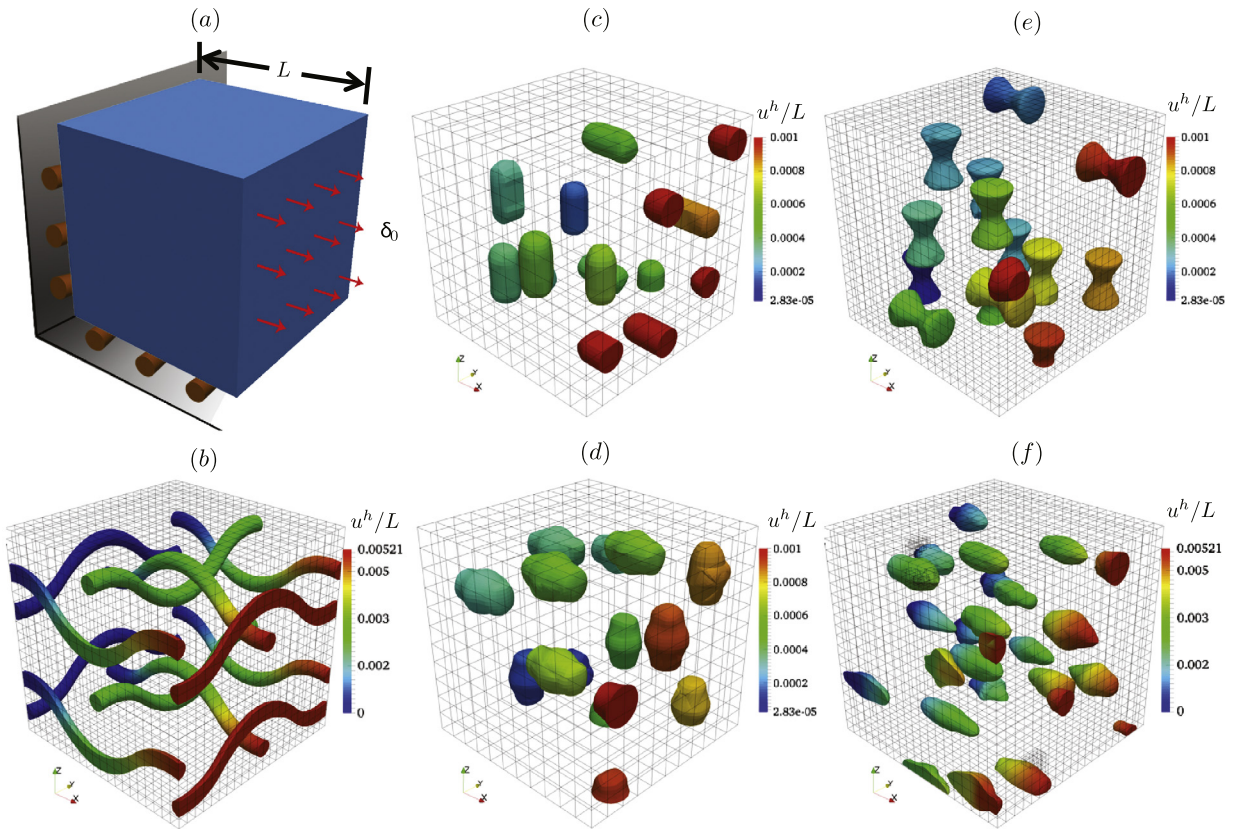

Fig. 10. (a) Domain geometry and boundary conditions used for the rest of application problems. (b–f) Contour plots for the displacement component u^h for different internal microstructures obtained by NIGFEM.

cavities. As apparent there, the NIGFEM captures the sharp variations of the solution fields in the vicinity of the cavities. As expected, the NIGFEM solution for stress vanishes when line A–B passes through cavities (denoted by ellipses in Fig. 9-f).

NIGFEM can also be used to capture the displacement and stress fields for heterogeneous materials with more complex internal microstructures as shown in the second set of examples presented in Fig. 10. Fig. 10-a shows the geometry and boundary conditions of a generic unit cell. A displacement δ_0 is applied to the right face of the domain and symmetry boundary conditions are used for the bottom and left faces. The remaining faces of the domain are chosen to be traction free. The elastic properties are $E_m = 2.4$ GPa and $\nu_m = 0.34$ for the matrix, and $E_i = 72$ GPa and $\nu_i = 0.22$ for the inclusions. For each problem, the domain is first discretized with structured mesh of hexahedral elements and then refined automatically as needed. It is worth mentioning that the choice of the number of elements (in each direction) for the non-conforming mesh dictates the number of refinement levels required in the subsequent solution step. Figs. 10c–f show the distribution of displacement component u^h obtained for each of these internal microstructures. The flexibility of the NURBS-enrichment used in the NIGFEM allows capturing a smooth solution for a variety of internal microstructures as well as fiber-shaped reinforcements (Fig. 10-b) and random-shaped particulate inclusions (Figs. 10c–f). For all these geometries, the structured NIGFEM mesh is created on the fly and the time needed to preprocess the mesh is only a fraction of the time needed to create conforming meshes associated with standard FE analyses.

5. Conclusions

The formulation and implementation of a NURBS-based interface-enriched GFEM method for solving 3D linear elasticity problems have been presented. The NIGFEM is well suited for problems with complex internal geometry, where the creation of conforming meshes is cumbersome. To capture the solution with non-conforming meshes, the NIGFEM utilizes NURBS to augment the finite element approximation space and minimize geometric errors. The use of NURBS in the enrichment of the finite element solution in the elements traversed by the material interfaces provides a natural and accurate way to capture the geometrical details of the internal microstructure. Convergence studies have shown that the NIGFEM has very good precision, and an optimal rate of convergence. The applications presented in the manuscript have illustrated the ability and efficiency of the method to simulate the structural response of a wide variety of heterogeneous materials with complex-shape inclusions.

Acknowledgements

This work has been supported by Grant No. FA9550-12-1-0445 to the Center of Excellence on Integrated Materials Modeling (CEIMM) at Johns Hopkins University (partners JHU, UIUC, UCSB), awarded by the AFOSR/RSL (Computational Mathematics Program, Manager Dr. A. Sayir) and AFRL/RX (Monitors Dr. C. Woodward and C. Przybyla).

References

[1] Y. Bazilevs, V. Calo, J. Cottrell, J. Evans, T. Hughes, S. Lipton, M. Scott, T. Sederberg, Isogeometric analysis using T-splines, Comput. Methods Appl. Mech. Eng. 199 (5–8) (2010) 229–263, http://dx.doi.org/10.1016/j.cma.2009.02.036, Computational Geometry and Analysis, http://www.sciencedirect.com/science/article/pii/S0045782509000875.

[2] A. Lewis, A. Geltmacher, Image-based modeling of the response of experimental 3D microstructures to mechanical loading, Scr. Mater. 55 (1) (2006) 81–85, http://dx.doi.org/10.1016/j.scriptamat.2006.01.043, viewpoint set no. 41 "3D Characterization and Analysis of Materials" Organized by G. Spanos, http://www.sciencedirect.com/science/article/pii/S1359646206000613.

[3] T. Kanit, S. Forest, I. Galliet, V. Mounoury, D. Jeulin, Determination of the size of the representative volume element for random composites: statistical and numerical approach, Int. J. Solids Struct. 40 (13–14) (2003) 3647–3679, http://dx.doi.org/10.1016/S0020-7683(03)00143-4, http://www.sciencedirect.com/science/article/pii/S0020768303001434.

[4] J.E. Bishop, J.M. Emery, R.V. Field, C.R. Weinberger, D.J. Littlewood, Direct numerical simulations in solid mechanics for understanding the macroscale effects of microscale material variability, Comput. Methods Appl. Mech. Eng. 287 (2015) 262–289, http://dx.doi.org/10.1016/j.cma.2015.01.017, http://www.sciencedirect.com/science/article/pii/S0045782515000377.

[5] J. Qian, Y. Zhang, W. Wang, A.C. Lewis, M.A.S. Qidwai, A.B. Geltmacher, Quality improvement of non-manifold hexahedral meshes for critical feature determination of microstructure materials, Int. J. Numer. Methods Eng. 82 (11) (2010) 1406–1423, http://dx.doi.org/10.1002/nme.2810.

[6] S.-B. Lee, G.S. Rohrer, A.D. Rollett, Three-dimensional digital approximations of grain boundary networks in polycrystals, Model. Simul. Mater. Sci. Eng. 22 (2) (2014) 025017, http://stacks.iop.org/0965-0393/22/i=2/a=025017.

[7] C.C. Wang, Direct extraction of surface meshes from implicitly represented heterogeneous volumes, Comput. Aided Des. 39 (1) (2007) 35–50, http://dx.doi.org/10.1016/j.cad.2006.09.003, http://www.sciencedirect.com/science/article/pii/S0010448506001837.

[8] Y. Zhang, T.J. Hughes, C.L. Bajaj, An automatic 3D mesh generation method for domains with multiple materials, Comput. Methods Appl. Mech. Eng. 199 (5–8) (2010) 405–415, http://dx.doi.org/10.1016/j.cma.2009.06.007, Computational Geometry and Analysis, http://www.sciencedirect.com/science/article/pii/S004578250900214X.

[9] R. Wentorf, R. Collar, M. Shephard, J. Fish, Automated modeling for complex woven mesostructures, Comput. Methods Appl. Mech. Eng. 172 (1–4) (1999) 273–291, http://dx.doi.org/10.1016/S0045-7825(98)00232-1, http://www.sciencedirect.com/science/article/pii/S0045782598002321.

[10] P. Young, T. Beresford-West, S. Coward, B. Notarberardino, B. Walker, A. Abdul-Aziz, An efficient approach to converting three-dimensional image data into highly accurate computational models, Philos. Trans. R. Soc. Lond. A, Math. Phys. Eng. Sci. 366 (1878) (2008) 3155–3173, http://dx.doi.org/10.1098/rsta.2008.0090.

[11] W.E. Lorensen, H.E. Cline, Marching cubes: a high resolution 3D surface construction algorithm, SIGGRAPH Comput. Graph. 21 (4) (1987) 163–169, http://dx.doi.org/10.1145/37402.37422, http://doi.acm.org/10.1145/37402.37422.

[12] Y. Zhang, C. Bajaj, B.-S. Sohn, 3D finite element meshing from imaging data, Comput. Methods Appl. Mech. Eng. 194 (48–49) (2005) 5083–5106, http://dx.doi.org/10.1016/j.cma.2004.11.026, Unstructured Mesh Generation, http://www.sciencedirect.com/science/article/pii/S0045782505000800.

[13] Y. Zhang, C. Bajaj, Adaptive and quality quadrilateral/hexahedral meshing from volumetric data, Comput. Methods Appl. Mech. Eng. 195 (9–12) (2006) 942–960, http://dx.doi.org/10.1016/j.cma.2005.02.016, http://www.sciencedirect.com/science/article/pii/S0045782505001374.

[14] N. Moës, M. Cloirec, P. Cartraud, J.-F. Remacle, A computational approach to handle complex microstructure geometries, Comput. Methods Appl. Mech. Eng. 192 (28–30) (2003) 3163–3177, http://dx.doi.org/10.1016/S0045-7825(03)00346-3, Multiscale Computational Mechanics for Materials and Structures, http://www.sciencedirect.com/science/article/pii/S0045782503003463.

[15] J. Dolbow, I. Harari, An efficient finite element method for embedded interface problems, Int. J. Numer. Methods Eng. 78 (2) (2009) 229–252, http://dx.doi.org/10.1002/nme.2486.

[16] T. Hettich, A. Hund, E. Ramm, Modeling of failure in composites by X-FEM and level sets within a multiscale framework, Comput. Methods Appl. Mech. Eng. 197 (5) (2008) 414–424, http://dx.doi.org/10.1016/j.cma.2007.07.017, http://www.sciencedirect.com/science/article/pii/S0045782507003258.

[17] J. Yvonnet, H. Le Quang, Q.-C. He, An XFEM/level set approach to modelling surface/interface effects and to computing the size-dependent effective properties of nanocomposites, Comput. Mech. 42 (1) (2008) 119–131, http://search.ebscohost.com/login.aspx?direct=true&db=a9h&AN=31428984&site=ehost-live.

[18] N. Sukumar, D.L. Chopp, N. Moës, T. Belytschko, Modeling holes and inclusions by level sets in the extended finite-element method, Comput. Methods Appl. Mech. Eng. 190 (46–47) (2001) 6183–6200, http://www.sciencedirect.com/science/article/pii/S0045782501002158.

[19] N. Sukumar, Z.Y. Huang, J.-H. Prévost, Z. Suo, Partition of unity enrichment for bimaterial interface cracks, Int. J. Numer. Methods Eng. 59 (8) (2004) 1075–1102, http://dx.doi.org/10.1002/nme.902.

[20] K.W. Cheng, T.-P. Fries, Higher-order XFEM for curved strong and weak discontinuities, Int. J. Numer. Methods Eng. 82 (5) (2010) 564–590, http://dx.doi.org/10.1002/nme.2768.

[21] R. Yuan, S.S. Singh, N. Chawla, J. Oswald, Efficient methods for implicit geometrical representation of complex material microstructures, Int. J. Numer. Methods Eng. 98 (2) (2014) 79–91, http://dx.doi.org/10.1002/nme.4619.

[22] A. Hansbo, P. Hansbo, An unfitted finite element method, based on Nitsche's method, for elliptic interface problems, Comput. Methods Appl. Mech. Eng. 191 (47–48) (2002) 5537–5552, http://dx.doi.org/10.1016/S0045-7825(02)00524-8, http://www.sciencedirect.com/science/article/pii/S0045782502005248.

[23] E. Burman, S. Claus, P. Hansbo, M.G. Larson, A. Massing, CutFEM: discretizing geometry and partial differential equations, Int. J. Numer. Methods Eng. 104 (7) (2015) 472–501, http://dx.doi.org/10.1002/nme.4823.

[24] S. Soghrati, A.M. Aragón, C. Armando Duarte, P.H. Geubelle, An interface-enriched generalized FEM for problems with discontinuous gradient fields, Int. J. Numer. Methods Eng. 89 (8) (2012) 991–1008, http://dx.doi.org/10.1002/nme.3273.

[25] S. Soghrati, H. Ahmadian, 3D hierarchical interface-enriched finite element method: implementation and applications, J. Comput. Phys. 299 (2015) 45–55, http://dx.doi.org/10.1016/j.jcp.2015.06.035, http://www.sciencedirect.com/science/article/pii/S0021999115004337.

[26] M. Safdari, A.R. Najafi, N.R. Sottos, P.H. Geubelle, A NURBS-based interface-enriched generalized finite element method for problems with complex discontinuous gradient fields, Int. J. Numer. Methods Eng. 101 (12) (2015) 950–964, http://dx.doi.org/10.1002/nme.4852.

[27] M.H. Tan, M. Safdari, A.R. Najafi, P.H. Geubelle, A NURBS-based interface-enriched generalized finite element scheme for the thermal analysis and design of microvascular composites, Comput. Methods Appl. Mech. Eng. 283 (2015) 1382–1400, http://dx.doi.org/10.1016/j.cma.2014.09.008, http://www.sciencedirect.com/science/article/pii/S004578251400317X.

[28] L.A. Piegl, W. Tiller, The Nurbs Book, 2nd edition, Monographs in Visual Communication, Springer-Verlag, New York, 1997, http://books.google.com/books?id=7dqY5dyAwWkC.
[29] D.F. Rogers, An Introduction to NURBS: With Historical Perspective, Academic Press, San Diego, 2000.
[30] R. Sevilla, S. Fernández-Méndez, A. Huerta, NURBS-enhanced finite element method (NEFEM), Arch. Comput. Methods Eng. 18 (4) (2011) 441–484.
[31] G. Haasemann, M. Kästner, S. Prüger, V. Ulbricht, Development of a quadratic finite element formulation based on the XFEM and NURBS, Int. J. Numer. Methods Eng. 86 (4–5) (2011) 598–617, http://dx.doi.org/10.1002/nme.3120.
[32] G. Legrain, A NURBS enhanced extended finite element approach for unfitted CAD analysis, Comput. Mech. 52 (4) (2013) 913–929.
[33] T. Belytschko, R. Gracie, G. Ventura, A review of extended/generalized finite element methods for material modeling, Model. Simul. Mater. Sci. Eng. 17 (4) (2009) 043001, http://stacks.iop.org/0965-0393/17/i=4/a=043001.
[34] A.R. Najafi, M. Safdari, D.A. Tortorelli, P.H. Geubelle, A gradient-based shape optimization scheme using an interface-enriched generalized FEM, Comput. Methods Appl. Mech. Eng. 296 (2015) 1–17, http://dx.doi.org/10.1016/j.cma.2015.07.024, http://www.sciencedirect.com/science/article/pii/S0045782515002455.
[35] S.E. Benzley, E. Perry, K. Merkley, B. Clark, G. Sjaardama, A comparison of all hexagonal and all tetrahedral finite element meshes for elastic and elasto-plastic analysis, in: Proceedings, 4th International Meshing Roundtable, vol. 17, Sandia National Laboratories, Albuquerque, NM, 1995, pp. 179–191.
[36] A. Tabarraei, N. Sukumar, Extended finite element method on polygonal and quadtree meshes, Comput. Methods Appl. Mech. Eng. 197 (5) (2008) 425–438, http://dx.doi.org/10.1016/j.cma.2007.08.013, Enriched Simulation Methods and Related Topics, http://www.sciencedirect.com/science/article/pii/S0045782507003374.
[37] A. Byfut, A. Schröder, hp-adaptive extended finite element method, Int. J. Numer. Methods Eng. 89 (11) (2012) 1392–1418, http://dx.doi.org/10.1002/nme.3293.
[38] T.-P. Fries, A. Byfut, A. Alizada, K.W. Cheng, A. Schröder, Hanging nodes and XFEM, Int. J. Numer. Methods Eng. 86 (4–5) (2011) 404–430, http://dx.doi.org/10.1002/nme.3024.
[39] A.K. Gupta, A finite element for transition from a fine to a coarse grid, Int. J. Numer. Methods Eng. 12 (1) (1978) 35–45, http://dx.doi.org/10.1002/nme.1620120104.
[40] J.N. Goodier, Concentration of stress around spherical inclusions and flaws, J. Appl. Mech. 1 (1933) 39–44.
[41] O.C. Zienkiewicz, J.Z. Zhu, The superconvergent patch recovery and a posteriori error estimates. Part 1: the recovery technique, Int. J. Numer. Methods Eng. 33 (7) (1992) 1331–1364, http://dx.doi.org/10.1002/nme.1620330702.
[42] L. Van Miegroet, P. Duysinx, Stress concentration minimization of 2D filets using X-FEM and level set description, Struct. Multidiscip. Optim. 33 (4–5) (2007) 425–438, http://dx.doi.org/10.1007/s00158-006-0091-1.
[43] T.-P. Fries, T. Belytschko, The extended/generalized finite element method: an overview of the method and its applications, Int. J. Numer. Methods Eng. 84 (3) (2010) 253–304, http://dx.doi.org/10.1002/nme.2914.
[44] C. Daux, N. Moës, J. Dolbow, N. Sukumar, T. Belytschko, Arbitrary branched and intersecting cracks with the extended finite element method, Int. J. Numer. Methods Eng. 48 (12) (2000) 1741–1760, http://dx.doi.org/10.1002/1097-0207(20000830)48:12<1741::AID-NME956>3.0.CO;2-L.
[45] N. Moës, A. Gravouil, T. Belytschko, Non-planar 3D crack growth by the extended finite element and level sets—Part I: mechanical model, Int. J. Numer. Methods Eng. 53 (11) (2002) 2549–2568, http://dx.doi.org/10.1002/nme.429.